ADVANCED MATERIALS TECHNOLOGIES
www.advmattechnol.de

Slow Photonic Effect Inducing Improved H_2 Generation in Photonic Films with Chiral Nematic Structure

*Masa Johar, Cong Wong, and Mohamed Nawfal Ghazzal**

Integrating photonic crystals (PCs) into the design of a photocatalyst can significantly enhance its light-harvesting capability. PCs can manipulate the propagation of light uniquely within a material and reduce its group velocity, thereby enhancing the absorption factor for photocatalysts. However, the slow photon effect in photoactive films with chiral nematic structures has not been reported yet, especially at the blue edge of the photonic bandgap. This work proposes a straightforward one-pot method to fabricate various photonic films with chiral nematic, namely g-C_3N_4/SiO_2, TiO_2/SiO_2, and g-C_3N_4/TiO_2/SiO_2. The sol-gel biotemplating formulation using cellulose nanocrystals successfully leads to the elaboration of films exhibiting variable iridescent colors with photonic bandgap from UV to visible range. The tunable wavelength of the Bragg peak reflection offers the opportunity to access a region with a slow photonic effect, which directly impacts the light-harvesting properties of the photoactive material. It is demonstrated that the H_2 generation is significantly enhanced when the blue edge of the photonic bandgap position overlapped with the absorbance band of the photocatalyst. These results offer the opportunity to design photonic materials with chiral nematic structure and optimize the photocatalytic performance for energy application.

1. Introduction

Light harvesting ability of photocatalysts is among the driving forces to reaching efficient conversion of solar energy to chemical fuel.[1] Huge efforts have been devoted to investigating new strategies that enhance the light-harvesting capabilities of semiconductors. These strategies can be broadly categorized into two main approaches: expanding the semiconductor's optical response across a wider spectral range and improving light–matter interactions. In the former approach, techniques such as doping with non-metallic ions[2–4] or transition metal cations,[5,6] incorporating noble metal nanoparticles,[7,8] sensitizing the semiconductor's,[7,9,10] and constructing heterojunction[11–14] have shown effectiveness. However, they face various challenges, including stability issues, increased recombination of charge carriers, weakened redox ability, selectivity, high costs, and toxicity concerns.[2,15–20] In the latter approach, constructing semiconductors in a hierarchical structure can manipulate light propagation within the semiconductor, prolong the time of light-matter interaction, enhance charge separation and provide more porous and active sites, thereby improving mass diffusion and transfer.[21–23] This approach is an effective strategy since the light-harvesting ability of semiconductor photocatalysts is strongly influenced by their structure.[24] Photons in a typical structure are in contact with a photoactive medium (thickness = 10 μm) for only a few hundred femtoseconds due to the speed of light ($1-3 \times 10^8$ m $^{-1}$s). Enhancing the time of light and semiconductor interaction is therefore crucial for improving light-harvesting capability and photoactivity. Inspired by Nature, PCs proposed by Yablonovich[25] and John[26] in 1987 have become a focal point of research due to their exceptional features. PCs, characterized by periodically ordered structural patterns with varying refractive indix, uniquely manipulate light propagation.[26–30] When light propagates within PCs, certain wavelengths of incident light cannot pass through the material; instead, they are reflected. These forbidden wavelengths are known as the photonic band gap or stop-band reflection. The range of reflected wavelengths depends on the intrinsic properties of the material, such as periodicity and dielectric contrast of the PCs. At the frequency edges of photonic bandgap (blue and red edges), the group velocity of the propagated photons is significantly reduced, a phenomenon referred to as the slow photon effect.[31–33] Integrating PCs into the design of a photocatalyst can significantly enhance light-harvesting capability. Once

M. Johar, C. Wong, M. N. Ghazzal
Université Paris-Saclay
UMR 8000 CNRS
Institut de Chimie Physique
Orsay 91405, France
E-mail: mohamed-nawfal.ghazzal@universite-paris-saclay.fr
M. Johar
Faculty of Science, Chemistry Department
An-Najah National University
Nablus 7, Palestine

The ORCID identification number(s) for the author(s) of this article can be found under https://doi.org/10.1002/admt.202302105

© 2024 The Authors. Advanced Materials Technologies published by Wiley-VCH GmbH. This is an open access article under the terms of the Creative Commons Attribution-NonCommercial License, which permits use, distribution and reproduction in any medium, provided the original work is properly cited and is not used for commercial purposes.

DOI: 10.1002/admt.202302105

the absorbance band of a photoactive material, designed in PCs, overlaps with the blue (red) edge of the PGB, an enhancement of the density of photogenerated charge carriers is observed.[34] The optical path length of photons and the time of their interaction with the photocatalyst increases at these edges, leading to an improved absorption factor (light-harvesting capabilities). The exceptional properties of PCs have driven many progress in a wide range of applications, such as waveguides,[35] dielectric mirrors,[36] sensors,[37] low threshold lasers,[38] etc. However, the propagation of light at the bandgap edges has recently attracted attention in solar conversion to energy applications.[39,40] The efficiency of slow photon-enhanced photocatalysis has been demonstrated in various studies. For example, Ozin et al. explained optically amplified photocatalytic reactions (photo-oxidation of adsorbed methylene blue) for anatase nanocrystals inverse opals with different macropore sizes by red edge slow photon effect.[41] In a similar vein, Liu et al showcased the enhanced photocatalytic efficiency of ZnO inverse opal by manipulating the angle of incident light to leverage the slow photon effect at the red edge.[42] Most studies believe the red edge is more useful for light-harvesting enhancement than the blue edge.[40] This is because of the primary localization of light in the high dielectric part of the PCs at the red edge and the low dielectric part at the blue edge.[39] However, a recent theoretical study by Deparis et al. proposes an alternative perspective, suggesting that slow photons at the blue edge can enhance light harvesting. This proposition is substantiated through rigorous coupled wave analysis simulation.[43] Notably, a few experimental studies have further confirmed the efficiency of the blue edge for H_2 generation.[44] Moreover, in most of the reported studies, PCs were prepared using polymeric spheres as a template. Thus, variable inverse opals films were prepared exhibiting amplified photocatalytic efficiency for dye degradation.[45–48] In this sense, the synthesis of photonic material is reaching a bottleneck. As an alternative, the elaboration of PCs using cellulose nanocrystals (CNCs) offers the possibility of creating a new generation of photoactive materials with a chiral nematic structure. CNCs is a green and cheap biotemplate that appears as a sustainable method for the synthesis of functional materials. Up to now, only a few studies reported the elaboration of nanostructured films using CNCs as biotemplate.[49–52] A lamellar structure has been obtained using the sol-gel process for TiO_2 films and other composite oxides. Indeed, the calcination process aiming at removing CNCs induces a change of the chiral nematic to a 1D lamellar structure due to coalescence of TiO_2 nanoparticles during the growth process. The chiral nematic structure was only maintained when hard templating method was used.[53,54]

In this work, we developed a straightforward one-pot method for designing PCs films, such as g-C_3N_4/SiO_2 (hereafter CN-CS), TiO_2/SiO_2 (hereafter CN-TS), and g-C_3N_4/TiO_2/SiO_2 (hereafter CN-CTS), for H_2 generation. The photoactive films exhibit replicas of a chiral nematic structure built using evaporation-induced self-assembly (EISA) of sol containing CNCs. The hybrid formulation, employing silica precursor in addition to adequate precursor of the photoactive photocatalyst (Titanium diidopropoxide bis acetylacetonate (TAA)and Urea), ensures the stabilization and transfer of the chiral nematic structure. The objective of this work is to demonstrate the slow photon enhancement effect on the photocatalytic activity of these three different systems, particularly at the blue edge of the photonic bandgap. The wavelength maximum of photonic bandgap was tuned by adjusting the sol formulation to control the pitch value of the chiral nematic structure, offering the opportunity to access the region where slow photon effect occurs without manipulating the incident light angle. Our results demonstrate the successful fabrication of iridescent chiral nematic films with tuneable Bragg peak reflection in the UV–vis range and confirm the efficiency of slow photons at the blue edge in the three different PCs systems for H_2 generation.

2. Results and Discussion

The photonic films were obtained by a cast of solution containing the TAA and Urea precursors for TiO_2 and g-C_3N_4 materials. To ensure the transfer and stability of the chiral nematic structure into the photonic films, we have included a certain amount of tetramethyl orthosilicate (TMOS), silica precursor, in the formulation. The silica will play a crucial role as a retarding of the crystallite growth of TiO_2 during the sintering process. The synthesis of hybrid mesoporous films began with multiple hydrolysis and polycondensation reactions of TAA and TMOS during the self-assembly process of CNCs. The solvent evaporation during the EISA process leads to an increase in the concentration of CNCs to a critical concentration that induces a phase transition from isotropic to anisotropic. Once the critical concentration is reached, CNCs undergo twisting along their helical axis, resulting in a stable liquid crystalline phase.[55] The crystalline liquid phase is characterized by the long-range order of the cellulose nanorods joined with a helical direction director that rotates 360° to create the twisted structure. The length of the helical axis over a 360° rotation is called the helical pitch, *P*. The self-organization of CNCs in solution goes through the formation of tactoids (the primitive components of liquid crystals) that merge and grow until the formation of long-range periodic ordered chiral nematic structure.[56,57] A concentration of 4 wt% CNCs solution was used as a biotemplate to construct the chiral nematic structure. This concentration is considered as a critical concentration for the onset isotropic phase to anisotropic phase transition.[49] The pH of the aqueous CNCs suspension was adjusted to 2.4 to achieve a homogeneous and stable sol of hydrolyzed TMOS, preserving the self-assembly of CNCs to form a chiral nematic structure.[58] Different amount of precursors was added to CNCs suspension to tune the *P* values (more details are provided in the experimental section, Table 1–3). The synthetic route and photographs of the synthesis are illustrated in **Figure** 1a,b. The mixtures were poured into polystyrene Petri dishes and left to dry for 48 hours, followed by calcination at 500 °C for 4 hours (Figure 1b). This temperature allows to remove CNCs, convert urea into g-C_3N_4 by polymerisation and form anatase TiO_2 phase. At the end, three distinct systems of films exhibiting chiral nematic structures and iridescent colors were successfully obtained (Figure 1b(I),(II)). The hybrid films are likely to shrink and crack as the concentration of the precursors increases, due to capillary stress gradients within the films induced by the polycondensation of the precursors. The obtained films exhibited various iridescent colors depending on the concentration of precursors. Some of the hybrid films appeared with the red color, while others were colorless, indicating the selective reflection in the visible and IR wavelength range

© 2024 The Authors. Advanced Materials Technologies published by Wiley-VCH GmbH

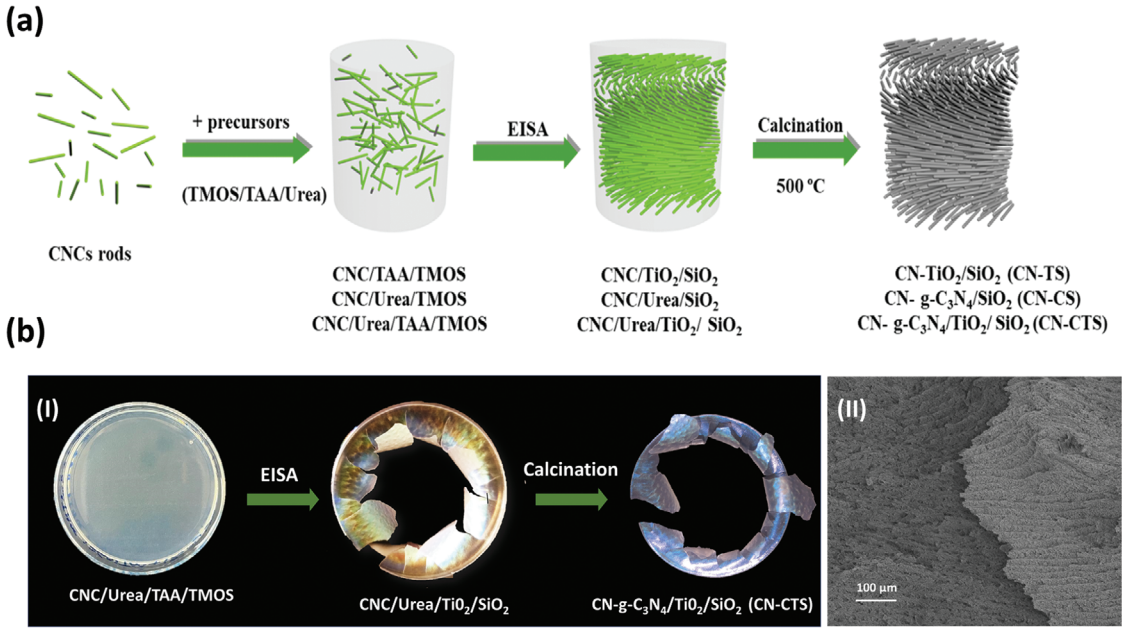

Figure 1. Synthetic route of CN-TS, CN-CS, and CN-CTS films derived from CNCs as a biotemplate and TMOS, urea, and TAA as precursors a). Photographs of the CN-CTS synthesis route b) (I). The cross-section image of CN-CTS highlights the presence of CN structure (b) (II).

(Figure S1d–f, Supporting Information). The maximum wavelength of the reflected light is defined by the Bragg law (Equation.1).

$$\lambda_{max} = n_{eff}\ \mathrm{P}\sin\theta \quad (1)$$

where n_{eff} is the effective refractive index, P is the pitch of the helical structure, and θ is the angle of the incident light.

The polarised optical microscope (POM) images of the resulting hybrid (Figure S1(a–b)) and calcined films (**Figure 2**a–c) show strong birefringence with dark and bright regions characteristic of periodic organization, allowing light deviation. After calcination of the hybrid films, the CNC template is removed, and the films maintain their iridescent colors. However, we observed a blue shift in the color of the calcined films compared to their hybrid counterparts, as shown in Figure 2. The color change arises from the removal of the biotemplate, which reduces the average refractive index of the films as CNCs are replaced by air. Indeed, the reflectance spectra, as shown in Figure 2d–f and Figure S1(d–f) (Supporting Information), are in agreement with the color observed for each film. The films reflect the light translated by Bragg reflection peaks (or photonic bandgap), and the wavelength maximum (λ_{max}) is redshifted from UV to visible range, as the amount of precursors increases. Calcined films with the lowest precursor loading exhibit a blue color with λ_{max} close to 480 nm, 420 nm, and 425 nm for CN-CS_1, CN-TS_1, and CN-CTS_1, respectively. A bluish-green color is observed for CN-TS_2 (487 nm) and CN-CTS_2 (490 nm), and a green color for CN-CS_2 (560 nm). A greenish-yellow color is observed for CN-TS_3 (550 nm), a yellow one for CN-CTS_3 (566 nm), and an orange color for CN-CS_3. The red color is reflected in films with the highest precursor loading, namely: CN-CS_4 (798 nm), CN-ST_4 (617 nm), and CN-CTS_4 (635 nm). Tuning the λ_{max} of the Bragg peak reflection across the UV–vis spectrum allows for the manipulation of interference between the blue edge of the photonic bandgap and the absorption spectrum of the photocatalyst. This manipulation facilitates access to the region where slow photon effect operates, which directly correlates with the light-harvesting capability of photocatalysts. The optical band gap of the films was estimated using a Tauc plot method (Figure S2, Supporting Information). The bandgap of CN-CS and CN-TS are similar to the electronic band gap of bulk g-C_3N_4 and anatase TiO_2, at 2.7 eV and 3.25 eV, respectively. However, the bandgap of the CN-CTS junction shows a slight increase in the value of bandgap towards the UV range (3.35 eV). This suggests that the ratios between TiO_2 and g-C_3N_4 might not have been sufficient to fine-tune the bandgap energy.

The cross-sections of hybrid and calcined films were characterized using scanning electron microscopy (SEM), and the images are presented in **Figure 3** and Figure S3a–f (Supporting Information). Periodically alternated layers of a twisted structure were observed along the film axis before and after calcination, a typical characteristic of chiral nematic structure. The removal of CNCs during calcination induces a reduction in the P value due to film shrinkage caused by polycondensation and dehydration of the polymeric network. The increase in ratios between precursors and CNCs in each photocatalytic system is evident in an increase in the distance between two adjacent layers (half helix pitch, $P/2$), as depicted in Figure 3a–f. As an example, the evolution of the half-pitch values which were measured for g-C_3N_4/TiO_2/SiO_2, and found to increase from 0.33 µm, 0.45 µm, and 1.3 µm for CN-CTS_1, CN-CTS_3, and CN-CTS_4, respectively. The increasing amount of precursors leads to an increase of helicoidal pitch P values, rationalizing the redshift of the photonic bandgap and the change in the iridescent colors of the calcined films.

© 2024 The Authors. Advanced Materials Technologies published by Wiley-VCH GmbH

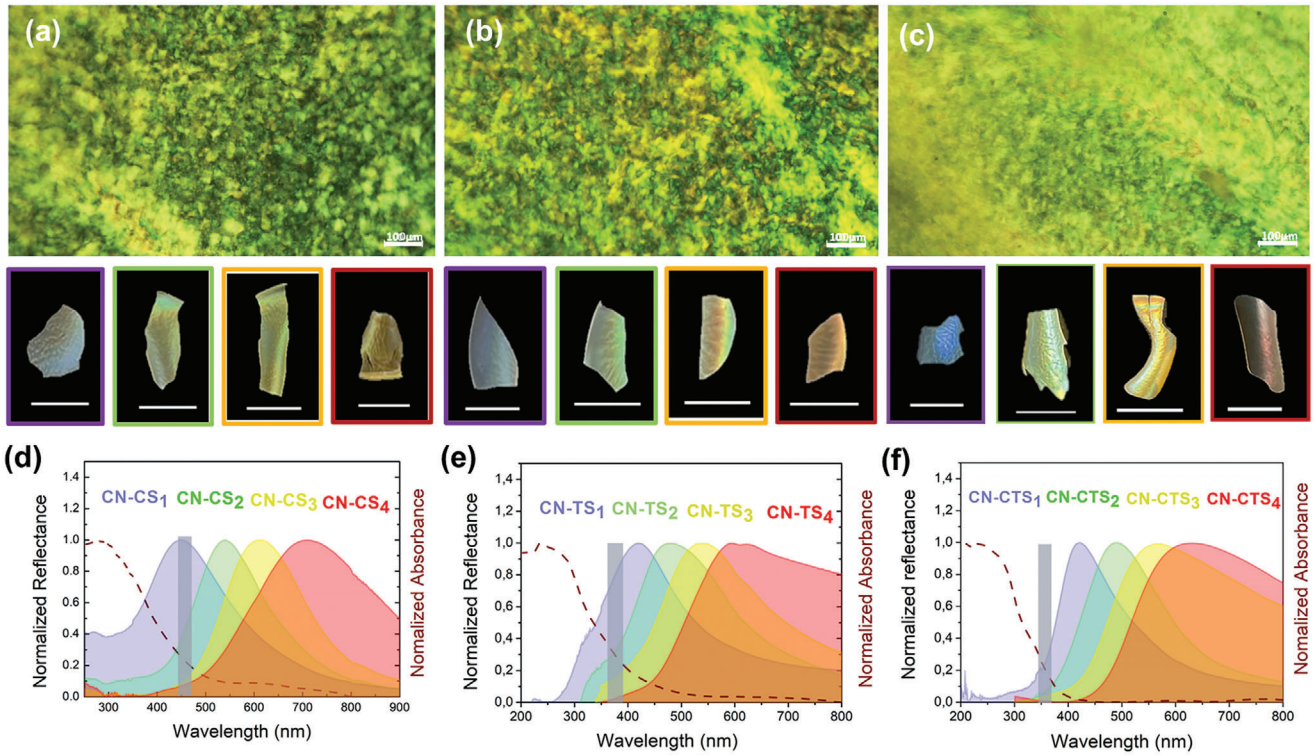

Figure 2. POM images of calcined films a) CN-CS_1 b) CN-TS_1, and c) CN-CTS_1. Photographs and UV–vis reflectance spectra of calcined films d) CN-CS e) CN-TS, and f) CN-CTS obtained with variable CNCs/precursors ratios and the corresponding absorption spectra. Dark blue rectangles represent the electronic band gap of each system. Scale bar = 1 cm.

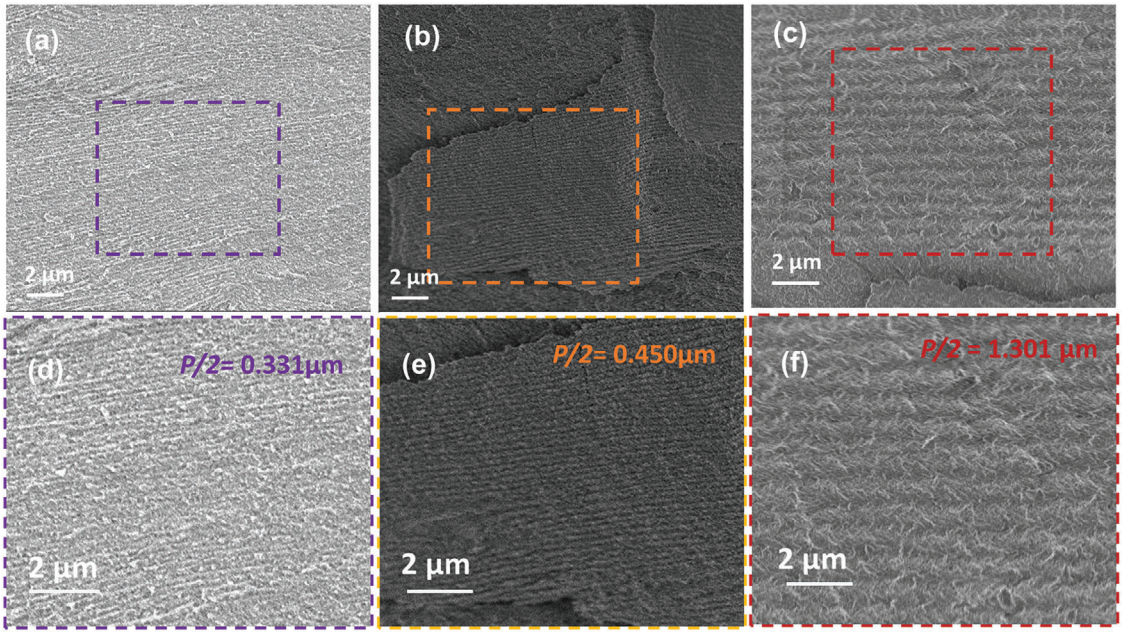

Figure 3. The cross-section images of CN-CTS_1 (a–d), CN-CTS_3 (b–e), and CN-CTS_4 films (c–f) with varying CNCs/precursors ratios, highlighting the increasing *P/2* values as the ratio increases.

© 2024 The Authors. Advanced Materials Technologies published by Wiley-VCH GmbH

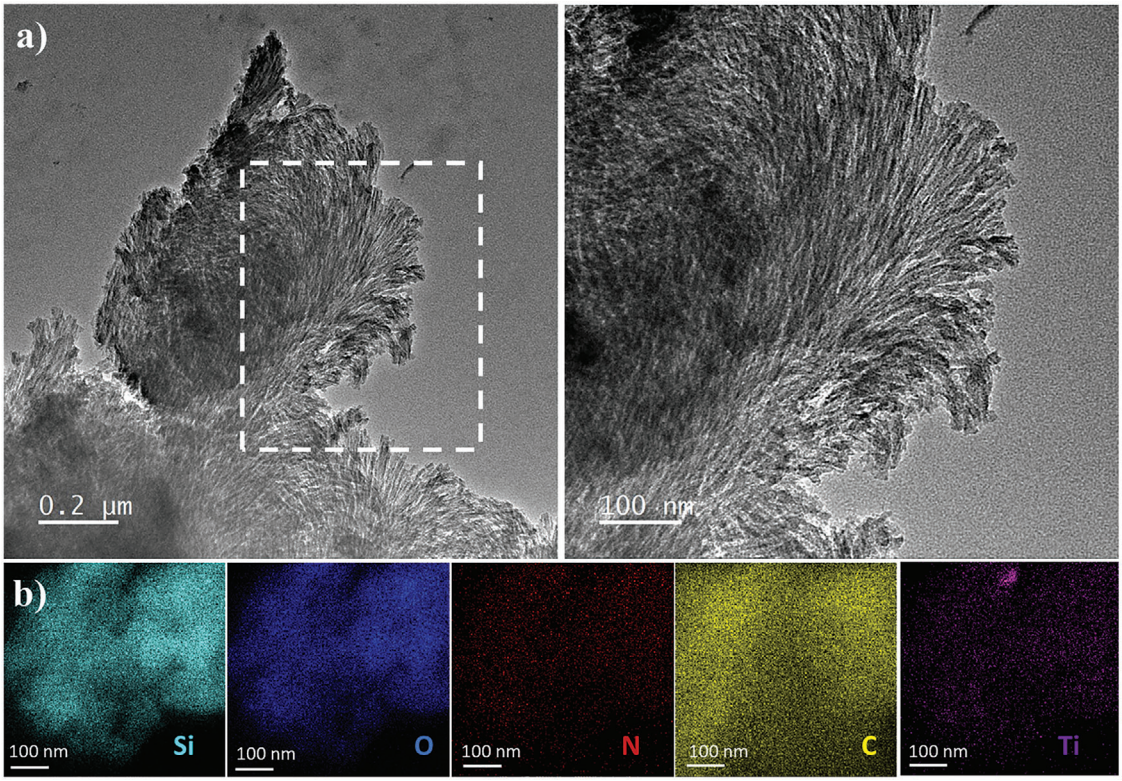

Figure 4. General view TEM images of CN-CTS$_3$ a), EDS compositional mapping of CN-CTS$_3$ b).

The morphology and chemical composition of the CN-CTS$_3$ calcined films were investigated using transmission electron microscopy (TEM) and energy dispersive X-ray spectroscopy (EDS) mapping as depicted in **Figure 4** and Figure S4 (Supporting information). The results revealed locally aligned rods twisting over the longitudinal axis (Figure 4a). The left-handed chiral nematic structure observed for the CN-CTS$_3$ films is typical of the one observed for silica films with chiral nematic structures reported in previous work.[58,59] The image indicates that the films are porous and are aligned in longitudinal order. The chemical composition of CN-CTS$_3$ was analyzed using EDS, and the results confirmed the presence of Ti, O, N, C, and Si. The elements are distributed throughout the films and overlap, as seen in Figure 4b.

The chemical surface compositions of CN-CS, CN-TS, and CN-CTS were further characterized using X-ray photoelectron spectroscopy (XPS). The survey confirms the presence of all principal elements (Ti, O, C, and Si) in their respective films (Figure S5a, Supporting Information), in agreement with EDS chemical mapping. The high-resolution C1s XPS spectra of CN-CS and CN-CTS are deconvoluted into four peaks (**Figure 5**a). The peaks centered at 284.7 and 286.4 eV can be assigned to C—C/C—H and C—O, respectively, while the peaks at 288.5 and 290.4 eV can be attributed to N—C = N bond in g-C_3N_4, respectively.[60,61] It should be noted that the deconvolution of the C1s peak of CN-TS showed three sub-peaks attributed to C-H/C-C, C-OH/C = C, and COO/C-O located at 284.8, 286.4 and 287.9 eV, respectively. The N1s high-resolution peak for CN-CS and CN-CTS is centered at 399.8 eV. The intensity of the peak is significantly lower for CN-CS compared to CN-CTS (Figure 5c; Figure S5c, Supporting Information). The peak recorded for CN-CTS is deconvoluted into two main peaks centered at 399.8 and 403.6 eV, attributed to C = N—C and N-(C)$_3$ in g-C_3N_4, in agreement with the reported studies.[62] It can be noticed that that no evidence for the presence of terminal amino groups at higher binding energies. High-resolution XPS spectra of Ti 2p region for CN-TS and CN-CTS display two peaks representing the spin-orbit components $2p_{3/2}$ and and $2p_{1/2}$ (Figure 5b).[63] The binding energy of the peaks is located at 465.6 eV and 459.9 eV, which are assigned to Ti^{4+} oxidation state (Ti—O—Ti bonding) of TiO_2.[64] The binding energy is positively shifted compared to Ti 2p in its anatase crystalline phase. The shift is even more pronounced in the case of CN-CTS. The shift points to the interaction between g-C_3N_4 and TiO_2 characterized by potential electron transfer and to the formation of a low Ti^{3+} valence state. Indeed, the shoulder of the Ti $2p_{3/2}$ peak could be assigned to the Ti^{3+} low valence state. The low valence state could be formed during the calcination step where silica and cellulose reduce the Ti^{4+} to Ti^{3+}. The energy difference between these spin-orbit components is equal to 5.68 eV and 5.71 eV consistent with the energy difference for Ti^{4+} in TiO_2.[65]

The photocatalytic efficiency of the films was evaluated by following the H_2 generation over illumination time. The samples were illuminated using a Mercury lamp for 5 h. **Figure 6**a displays the H_2 accumulated during the irradiation time for CN-CS, CN-CTS, and CN-TS films. The photocatalytic H_2 generation was found to vary regarding the evolution of the ratio of the precursors into the films. The optimal combination for H_2 generation is CN-CS$_3$, CN-TS$_1$, and CN-CTS$_1$, in which 60, 36.5, and

© 2024 The Authors. Advanced Materials Technologies published by Wiley-VCH GmbH

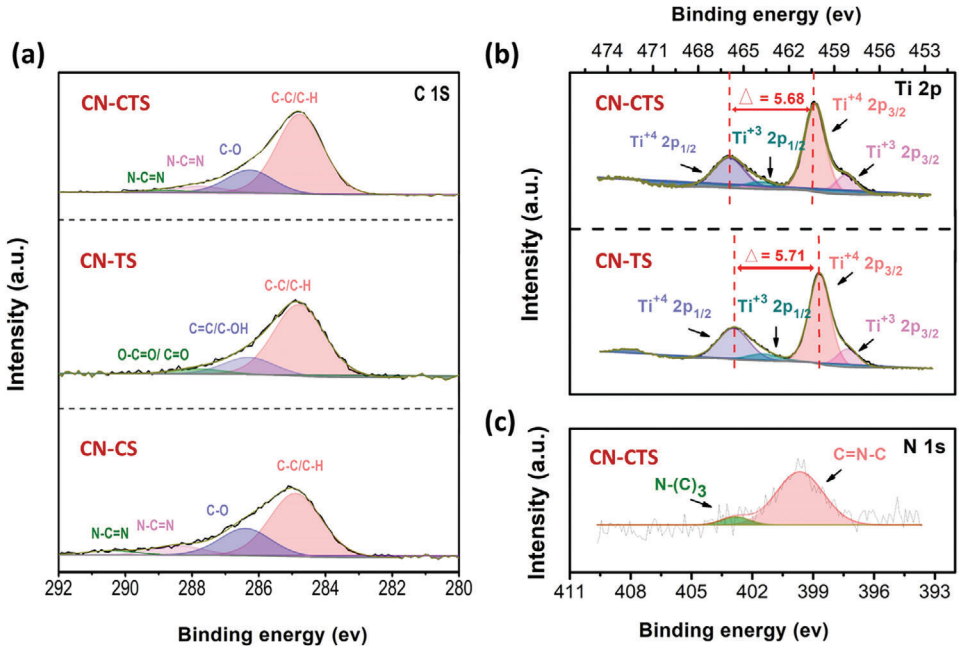

Figure 5. High resolution XPS spectra of C 1s of CN-CTS, CN-TS and CN-CS films a), Ti 2P of CN-CTS and CN-TS films b), and N 1s of CN-CTS films c).

34.2 μmol g^{-1} are produced, respectively. The H_2 kinetic rate constants are 12.94 (CN-CS_3), 7.872 (CN-TS_1), and 7.31(CN-CTS_1) μmol g^{-1} h^{-1}, as depicted in Figure 6b. It is worth noting that an increase in the amount of photocatalysts does not necessarily lead to higher H_2 generation. Indeed, the formulation ensures maintaining the same ratio between each precursor while increasing the overall amount of precursors. To understand the photocatalytic efficiency of each system, we investigated the overlap of the absorbance band of the films with the blue edge of the photonic bandgap. The dark blue rectangles represent the electronic bandgap of CN-CS, CN-TS, and CN-CTS as seen in the UV-vis reflection spectra (Figure 2d–f). Tuning λ_{max} of the photonic bandgap in each system (by increasing the pitch) offers the opportunity to have an overlap between the blue edge and the absorbance band of the films, which in turn, accesses the region of slow photon effect. For instance, in the CN-CS system, CN-CS_3 shows an obvious overlapping between the blue edge of its photonic bandgap and its electronic bandgap. Therefore, under light irradiation, the photon velocity slows down significantly inside the structure, increasing the time of light-matter interaction and subsequently lead to more electron-holes generation and a higher light absorption factor. In fact, the absorbance of the light increases in this specific region as reported by Deparis et al.[43] As a result, CN-CS_3 exhibits higher photocatalytic activity compared to other CN-CS films. The blue edge of CN-CS_4 is also aligned with the electronic band gap of CN-CS, although not to the extent observed in CN-CS_3. This observation can elucidate the rationale behind the superior activity of CN-CS_4 over CN-CS_2 and CN-CS_1 films. CN-CS_1 demonstrates the lowest photocatalytic activity, despite its photonic bandgap overlapping with the electronic band gap of CN-CS. To comprehend its behavior, it is crucial to note that while the blue edge of the photonic bandgap overlaps with the absorbance band, the maximum of the Bragg peak reflection also overlaps with the absorbance region. In this specific case, the slow photon effect is not the dominant factor in PCs. The reflection of forbidden wavelength must be considered to fully understand photocatalytic activity. In the case of CN-CS_1, light reflection lowers the light absorption, resulting in decreased photocatalytic activity. CN-TS_1 exhibits higher photocatalytic activity among all, despite the slow photon effect presented in CN-TS_2. This can be attributed to the full match of CN-TS_1 blue edge with the absorption spectrum of CN-TS, where the absorption reaches the maximum. As the blue edge of the photonic bandgap shifts to a higher wavelength by increasing the amount of the precursors, the photocatalytic H_2 generation decreases. In the heterojunction system (CN-CTS), even though there is no significant enhancement of the photocatalytic activity compared with individual counterparts as expected, the phenomenon of slow photon effect was also proved. CN-CTS_1 shows the best photocatalytic activity as overlapping between its photonic bandgap blue edge and the electronic band gap is observed. Overall, in variable films where the photonic bandgap is tuned from the UV to the visible light, a slow photonic effect can be observed as the enhancement of the photocatalytic activity occurs, regardless of the photocatalyst used. Cyclic stability test was performed for CN-TS_1 and CN-CS_3 films, both show a decrease in their stability by time, around 30% and 60% of the total activity were lost after 4 cycles, respectively (Figure S6, Supporting Information).

To further clarify the enhanced improvement resulting from the blue-edge slow photon effect, we examined the photoluminescence (PL) spectra of the CN-CS, CN-TS, and CN-CTS films. In general, the PL signal probes the separation of photogenerated charge carriers as a consequence of the recombination of electrons (e^-) and holes (h^+).[66] The intensity of the PL spectrum reflects the recombination rate of e^-/h^+ or the number of photogenerated charge carriers.[67–69] Since the formulation of each system ensures the maintenance of the same ratio between each precursor, we believe that in each system, all films exhibit the

© 2024 The Authors. Advanced Materials Technologies published by Wiley-VCH GmbH

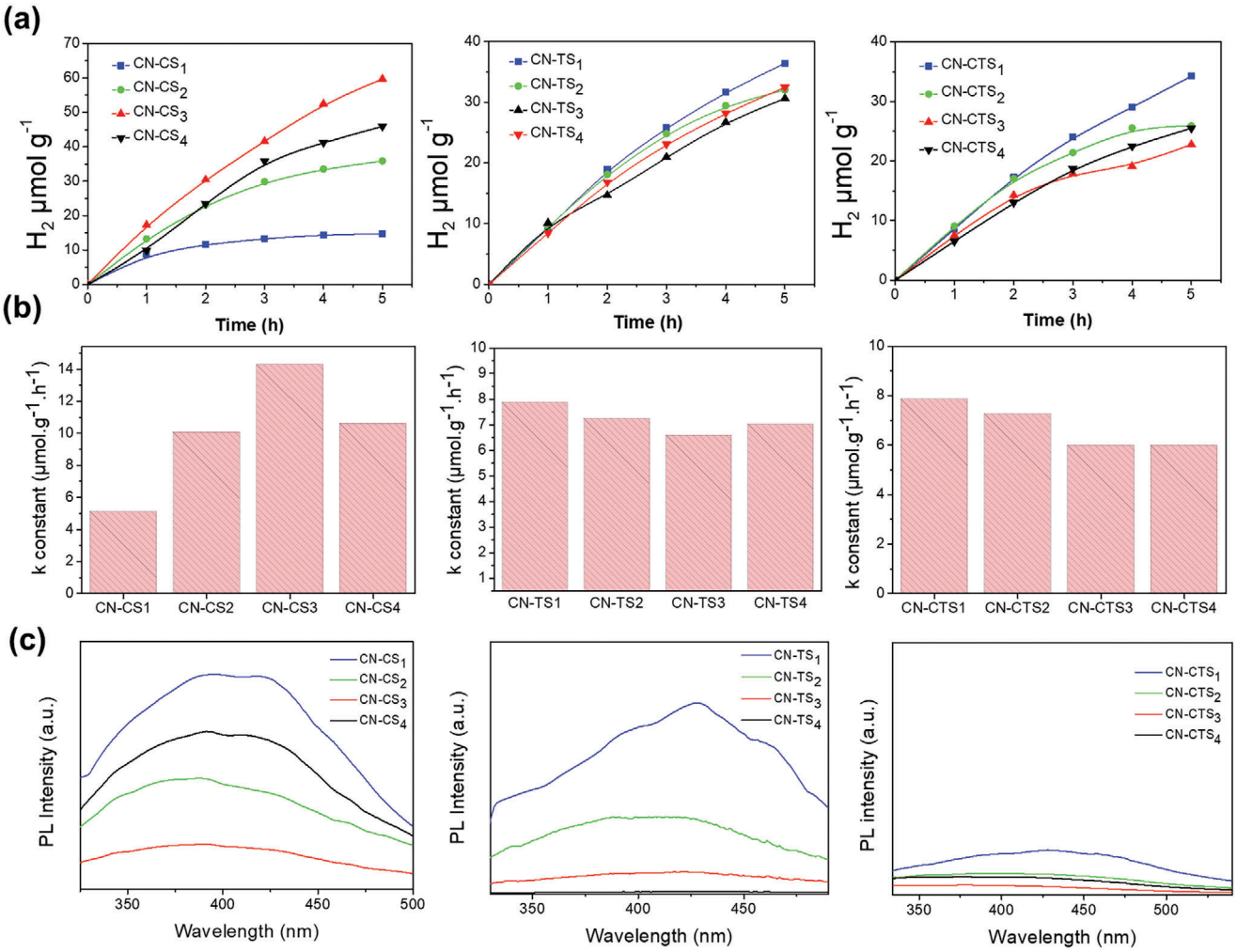

Figure 6. a) H_2 generation test b) Rate constants of H_2 generation for CN-CS, CNs-TS, and CN- CTS films c) PL spectra measured at λ_{ex} = 300 nm for CN-CS, CNs-TS, and CN- CTS films.

same recombination rate of e^-/h^+ regardless of the *P* values. Therefore, the PL intensity can represent the number of photogenerated charge carriers in these films. Figure 6c presents the PL spectra of all films excited at 300 nm. The CN-CS_1, CN-ST_1, and CN-CTS_1 films exhibit higher PL intensity compared to the other films, indicating a higher density of photogenerated charge carriers. In this experiment, the blue edges of these films overlap with the excitation wavelength and the absorption spectrum of each system, leading to higher light absorption due to the slow photon effect.

3. Conclusion

This study focuses on exploiting the advantages of photonic crystals with chiral nematic structure, particularly the slow photon effect, to enhance the light-harvesting capabilities of photocatalysts. Our work presents a novel one-pot method for fabricating three distinct chiral nematic photonic crystal films compsed of TiO_2/SiO_2, g-C_3N_4/SiO_2, and g-$C_3N_4/TiO_2/SiO_2$ Through the combination of sol-gel chemistry and cellulose nanocrystals as biotemplate, we achieved films with controllable photonic bandgaps, demonstrating iridescent colors. Importantly, the tunability is achieved without manipulating incident light angles. The ability to adjust the photonic bandgap position allows us to explore the slow photon effect, especially at the blue edge. Our findings emphasize the significant impact of adjusting the blue edge of the photonic bandgap position on the photocatalyst's performance for H_2 generation, showcasing the effective utilization of the slow photon effect.

4. Experimental Section

Materials: Cellulose nanocrystals (CNCs, 4wt%) were used without further purification, tetramethyl orthosilicate (TMOS, 99.9%), titanium diidopropoxide bis (acetylacetonate) (TAA, 75wt%) in isopropanol, urea, ethanol (≥99.9%), sulfuric acid (H_2SO_4, 95–98%), Mill-Q water under 18.2 MΩ. All reagents were bought from Sigma-Aldrich except CNCs were bought from University of MAINE.

Fabrication of Chiral Nematic TiO_2/SiO_2 (CN-TS) Films: Typically, 5 mL of diluted aqueous CNCs suspension (4 wt%, pH = 2.4, adjusted by

© 2024 The Authors. Advanced Materials Technologies published by Wiley-VCH GmbH

H_2SO_4) were mixed with different volumes of TMOS (0.6, 0.7, 0.8 and 0.9 ml). The mixtures were stirred at room temperature to form homogeneous solutions. Then, 24 µl, 28 µl, 32 µl and 36 µl TAA were dissolved in 1 ml ethanol and added respectively into CNCs/TMOS mixtures, followed by stirring for 20 min. Last, the homogeneous bright yellow mixtures were poured into polystyrene Petri dishes (diameter = 5.5 cm) and left to dry at room temperature for about 48 h to obtain iridescent hybrid films. The resulting hybrid films were then calcined in air at a heating rate of 2 °C /min to 500 °C for 4 h, yielding iridescent chiral nematic TiO_2/SiO_2 films. The following table summarizes the name and the amount of each material used (**Table 1**).

Fabrication of Chiral Nematic g-C_3N_4 /SiO_2 (CN-CS) Films: Different amounts of urea (120, 140, 160, and 180 mg) were dissolved in 5 mL of diluted aqueous CNCs suspension (4 wt%, pH = 2.4, adjusted by H_2SO_4). The mixtures were stirred for a few minutes and mixed with different volumes of TMOS (0.6, 0.7, 0.8, and 0.9 ml) respectively, followed by stirring for 20 min. Lastly, the homogeneous mixtures were poured into polystyrene Petri dishes (diameter = 5.5 cm) and left to dry at room temperature for about 48 h to obtain iridescent CNC/Urea/SiO_2 hybrid films. The resulting hybrid films were then calcined in air at a heating rate of 2 °C min^{-1} to 500 °C for 4 h, yielding iridescent chiral nematic g-C_3N_4/SiO_2films. The following table summarizes the name and the amount of each material used (**Table 2**).

Fabrication of Chiral Nematic g-C_3N_4/TiO_2 /SiO_2(CN-CTS) Films: Different amounts of urea (120, 140, 160, and 180 mg) were dissolved in 5 mL of diluted aqueous CNCs suspension (4 wt%, pH = 2.4, adjusted by H_2SO_4). The mixtures were stirred for a few minutes and mixed with different volumes of TMOS (0.6, 0.7, 0.8, and 0.9 ml) respectively, followed by stirring for 20 min. Then, 24 µl, 28 µl, 32 µl and 36 µl TAA were dissolved in 1 ml ethanol and added respectively into CNCs/Urea/TMOS mixtures, followed by stirring for 20 min. Lastly, the homogeneous bright yellow mixtures were poured into polystyrene Petri dishes (diameter = 5.5 cm) and left to dry at room temperature for about 48 h to obtain iridescent CNC/Urea/TiO_2/SiO_2 hybrid films. The resulting hybrid films were then calcined in air at a heating rate of 2 °C min^{-1} to 500 °C for 4 h, yielding iridescent chiral nematic g-C_3N_4/TiO_2/SiO_2 films (**Table 3**).

Photocatalytic Hydrogen Evolution Test: The hydrogen generation experiments were carried out in a closed quartz reactor. Inside the reactor, 80 mg of the calcined photocatalyst films were cracked into small pieces and added into 15 ml aqueous solution containing 5 ml of triethanolamine (TEOA). The reactor was degassed by nitrogen gas for 30 minutes to remove dissolved oxygen. All samples were irradiated by a mercury lamp (150 mV) for 5 h and under stirring. During irradiation, the gas production was taken from the reactor after each one hour and analyzed by gas chromatography (Micro GC Fusion).

Table 1. Summarization of CN-TS names and precursor volumes.

Film name	CNC [ml]	TMOS [ml]	TAA [µl] in 1 ml EtOH
CN-TS_1	5	0.6	24
CN-TS_2	5	0.7	28
CN-TS_3	5	0.8	32
CN-TS_4	5	0.9	36

Table 2. Summarization of CN-CS names and precursor.

Film name	CNC [ml]	TMOS [ml]	Urea [mg]
CN-CS_1	5	0.6	120
CN-CS_2	5	0.7	140
CN-CS_3	5	0.8	160
CN-CS_4	5	0.9	180

Table 3. Summarization of CN-TS names and precursor volumes.

Film name	CNC [ml])	TMOS [ml]	Urea [mg]	TAA [µl] in 1 ml EtOH
CN-TS_1	5	0.6	120	24
CN-TS_2	5	0.7	140	28
CN-TS_3	5	0.8	160	32
CN-TS_4	5	0.9	180	36

Characterizations: *UV–vis-NIR Spectrophotometer*: Optical properties of the calcined films were analyzed by UV–vis spectroscopy (model Cary 5000 series, Agilent Technologies) equipped with an integrating sphere for diffuse and total reflection measurements. The films were mounted perpendicular to the beam light in order to record diffusion reflectance spectra (DRS). The maximum reflectance was set to 100% using $BaSO_4$ as a reference in a wavelength range between 200 and 800 nm. Absorption spectra of the CN-CS, CN-TS, CN-CTS films were recorded after cracking using the same UV–vis NIR spectrophotometer.

Scanning Electron Microscopy (SEM): The structural properties of the calcined films were studied by SEM. It was used to carry out imaging on film cross-sections. SEM images were obtained with a ZEISS Supra 55VP FEG-SEM operating at a voltage of 2 kV and with a working distance between 4 and 7 mm.

Transmission Electron Microscopy (TEM): The morphology of the calcined films was analyzed using TEM, JEOL JEM 2100Plus, operating at 200 kV. The calcined films were cracked into small pieces and dispersed in ethanol solution, then drop-casting on Nickle grids and left for drying before analysis. Energy dispersive X-ray (EDX) spectroscopy was carried out at 200 kV in scanning TEM (STEM) mode.

Polarizing Optical Microscopy (POM): The texture of hybrid and calcined films was studied between crossed polarizers on a Zeiss Axio-Observer equipped with a ZEISS Axiocam 208 color.

Photoluminescence Spectroscopy (PL): PL spectra were recorded at 300 nm excitation with a Fluorolog 3 HORIBA fluorimeter. The emission spectra were monitored in 360–600 nm range.

Statistical Analysis: All figures were plotted by Origin software. A normalization was done for the Y-axis of Figure 2c. The half-pitch values (*P*/2) were measured by imageJ software. Each value corresponds to the average value of 100 measurements.

Acknowledegments

M.J. and C.W. contributed equally to this work. M.J. acknowledges Campus France and An-Najah National University for their joint scholarship to follow her research position. The authors were thankful to François Brisset for capturing the SEM and TEM images and Marie-Claire Schanne-Klein for providing full access to the polarized optical microscope.

Supporting Information

Supporting Information is available from the Wiley Online Library or from the author.

Conflict of Interest

The author declare no conflict of interest.

Data Availability Statement

The data that support the findings of this study are available from the corresponding author upon reasonable request.

© 2024 The Authors. Advanced Materials Technologies published by Wiley-VCH GmbH

Keywords

cellulose nanocrystals, chiral nematic structure, g-C_3N_4 , H_2 production, photonic band gap, photonic crystals, slow photon effect, TiO_2

Received: December 7, 2023
Revised: March 15, 2024
Published online:

[1] C. Wang, M. N. Ghazzal, *Energy Adv.* **2023**, *2*, 965.
[2] J. C. Yu, H. O. Yu, Z. Jiang, *Chem. Mater.* **2002**, *14*, 3808.
[3] J. Kwon, K. Choi, M. Schreck, T. Liu, E. Tervoort, M. Niederberger, *ACS Appl. Mater. Interfaces* **2021**, *13*, 53691.
[4] T. Umebayashi, T. Yamaki, H. Itoh, K. Asai, *Appl. Phys. Lett.* **2002**, *81*, 454.
[5] W. Choi, A. Termin, M. R. Hoffmann, *J. Phys. Chem.* **1994**, *98*, 13669.
[6] K. E. Karakitsou, X. E. Verykios, *J. Phys. Chem.* **1993**, *97*, 1184.
[7] J. Hensel, G. Wang, Y. Li, J. Z. Zhang, *Nano Lett.* **2010**, *10*, 478.
[8] A. Furube, L. Du, K. Hara, R. Katoh, M. Tachiya, *J. Am. Chem. Soc.* **2007**, *129*, 14852.
[9] Z.-S. Wang, C.-H. Huang, Y.-Y. Huang, Y.-J. Hou, P.-H. Xie, B.-W. Zhang, H.-M. Cheng, *Chem. Mater.* **2001**, *13*, 678.
[10] M. Quintana, T. Edvinsson, A. Hagfeldt, G. Boschloo, *J. Phys. Chem. C* **2007**, *111*, 1035.
[11] J. Li, X. Han, D. Wang, L. Zhu, M. Ha-Thi, T. Pino, J. Arbiol, L. Wu, M. Nawfal Ghazzal, *Angew. Chem.* **2022**, *134*, 202210242.
[12] J. Li, Z. Huang, C. Wang, L. Tian, X. Yang, R. Zhou, M. N. Ghazzal, Z.-Q. Liu, *Appl. Catal., B* **2024**, *340*, 123181.
[13] J. Li, H. Fang, M. Wu, C. Ma, R. Lian, S. P. Jiang, M. N. Ghazzal, Z. Rui, *Small* **2023**, *35*, 2300559.
[14] J. Li, A. Slassi, X. Han, D. Cornil, M. Ha-Thi, T. Pino, D. P. Debecker, C. Colbeau-Justin, J. Arbiol, J. Cornil, *Adv. Funct. Mater.* **2021**, *31*, 2100994.
[15] L. Li, J. Yan, T. Wang, Z.-J. Zhao, J. Zhang, J. Gong, N. Guan, *Nat. Commun.* **2015**, *6*, 5881.
[16] E. M. Samsudin, S. B. Abd Hamid, *Appl. Surf. Sci.* **2017**, *391*, 326.
[17] X. Chen, S. S. Mao, *Chem. Rev.* **2007**, *107*, 2891.
[18] D. Ren, W. Zhang, Y. Ding, R. Shen, Z. Jiang, X. Lu, X. Li, *Sol. RRL* **2020**, *4*, 1900423.
[19] Q. Xu, B. Zhu, C. Jiang, B. Cheng, J. Yu, *Sol. RRL* **2018**, *2*, 1800006.
[20] J. Tian, J. Zhang, X. Li, B. Cheng, J. Yu, W. Ho, *Sol. RRL* **2020**, *4*, 2000090.
[21] X. Li, J. Yu, M. Jaroniec, *Interface Sci. Technol.* **2020**, *31*, 1.
[22] X. Li, J. Yu, M. Jaroniec, *Chem. Soc. Rev.* **2016**, *45*, 2603.
[23] X.-Y. Yang, L.-H. Chen, Y. Li, J. C. Rooke, C. Sanchez, B.-L. Su, *Chem. Soc. Rev.* **2017**, *46*, 481.
[24] M. Xiao, Z. Wang, M. Lyu, B. Luo, S. Wang, G. Liu, H. Cheng, L. Wang, *Adv. Mater.* **2019**, *31*, 1801369.
[25] E. Yablonovitch, *Phys. Rev. Lett.* **1987**, *58*, 2059.
[26] S. John, *Phys. Rev. Lett.* **1987**, *58*, 2486.
[27] K. Ishizaki, K. Suzuki, S. Noda, *MDPI* **2016**, *3*, 36.
[28] E. Armstrong, C. O'Dwyer, *J. Mater. Chem. C* **2015**, *3*, 6109.
[29] J. F. Galisteo-López, M. Ibisate, R. Sapienza, L. S. Froufe-Pérez, Á. Blanco, C. López, *Adv. Mater.* **2011**, *23*, 30.
[30] C. Duan, Z. Cheng, B. Wang, J. Zeng, J. Xu, J. Li, W. Gao, K. Chen, *Small* **2021**, *17*, 2007306.
[31] J. I. L. Chen, G. von Freymann, S. Y. Choi, V. Kitaev, G. A. Ozin, *Adv. Mater.* **2006**, *18*, 1915.
[32] A. Imhof, W. L. Vos, R. Sprik, A. Lagendijk, *Phys. Rev. Lett.* **1999**, *83*, 2942.
[33] M. Ren, R. Ravikrishna, K. T. Valsaraj, *Environ. Sci. Technol.* **2006**, *40*, 7029.
[34] J. I. L. Chen, G. von Freymann, S. Y. Choi, V. Kitaev, G. A. Ozin, *Adv. Mater.* **2006**, *18*, 1915.
[35] M. Lončar, T. Doll, J. Vučković, A. Scherer, *J. Lightwave Technol.* **2000**, *18*, 1402.
[36] V. Agarwal, J. Del Rıo, *Appl. Phys. Lett.* **2003**, *82*, 1512.
[37] T. Li, G. Liu, H. Kong, G. Yang, G. Wei, X. Zhou, *Coord. Chem. Rev.* **2023**, *475*, 214909.
[38] D. P. Puzzo, F. Scotognella, M. Zavelani-Rossi, M. Sebastian, A. J. Lough, I. Manners, G. Lanzani, R. Tubino, G. A. Ozin, *Nano Lett.* **2009**, *9*, 4273.
[39] S. Nishimura, N. Abrams, B. A. Lewis, L. I. Halaoui, T. E. Mallouk, K. D. Benkstein, J. Van de Lagemaat, A. J. Frank, *J. Am. Chem. Soc.* **2003**, *125*, 6306.
[40] J. Liu, H. Zhao, M. Wu, B. Van Der Schueren, Y. Li, O. Deparis, J. Ye, G. A. Ozin, T. Hasan, B.-L. Su, *Adv. Mater.* **2017**, *29*, 1605349.
[41] J. I. L. Chen, G. von Freymann, S. Y. Choi, V. Kitaev, G. A. Ozin, *Adv. Mater.* **2006**, *18*, 1915.
[42] J. Liu, J. Jin, Y. Li, H.-W. Huang, C. Wang, M. Wu, L.-H. Chen, B.-L. Su, *J. Mater. Chem. A* **2014**, *2*, 5051.
[43] O. Deparis, S. R. Mouchet, B.-L. Su, *Phys. Chem. Chem. Phys.* **2015**, *17*, 30525.
[44] H. Zhao, Z. Hu, J. Liu, Y. Li, M. Wu, G. Van Tendeloo, B.-L. Su, *Nano Energy* **2018**, *47*, 266.
[45] T. L. Madanu, L. Chaabane, S. R. Mouchet, O. Deparis, B.-L. Su, *J. Colloid Interface Sci.* **2023**, *647*, 233.
[46] L. Zhang, C. Lin, V. K. Valev, E. Reisner, U. Steiner, J. J. Baumberg, *Small* **2014**, *10*, 3970.
[47] L. Zhang, C. Baumanis, L. Robben, T. Kandiel, D. Bahnemann, *Small* **2011**, *7*, 2714.
[48] X. Zhang, Y. Liu, S.-T. Lee, S. Yang, Z. Kang, *Energy Environ. Sci.* **2014**, *7*, 1409.
[49] C. Wang, J. Li, E. Paineau, A. Laachachi, C. Colbeau-Justin, H. Remita, M. N. Ghazzal, *J. Mater. Chem. A* **2020**, *8*, 10779.
[50] T.-D. Nguyen, E. Lizundia, M. Niederberger, W. Y. Hamad, M. J. MacLachlan, *Chem. Mater.* **2019**, *31*, 2174.
[51] G. D. Gesesse, C. Li, E. Paineau, Y. Habibi, H. Remita, C. Colbeau-Justin, M. N. Ghazzal, *Chem. Mater.* **2019**, *31*, 4851.
[52] Y. Li, J. Jun-Yan Suen, E. Prince, E. M. Larin, A. Klinkova, H. Thérien-Aubin, S. Zhu, B. Yang, A. S. Helmy, O. D. Lavrentovich, E. Kumacheva, *Nat. Commun.* **2016**, *7*, 12520.
[53] K. E. Shopsowitz, A. Stahl, W. Y. Hamad, M. J. MacLachlan, *Angew. Chem.* **2012**, *124*, 6992.
[54] C. Li, E. Paineau, F. Brisset, S. Franger, C. Colbeau-Justin, M. N. Ghazzal, *Catal. Today* **2019**, *335*, 409.
[55] T. Abitbol, E. D. Cranston, in *Handbook of Green Materials: 3 Self- and Direct-Assembling of Bionanomaterials*, World Scientific, Singapore **2014**, pp. 37–56.
[56] P.-X. Wang, W. Y. Hamad, M. J. MacLachlan, *Nat. Commun.* **2016**, *7*, 11515.
[57] C. Wang, E. Paineau, H. Remita, M. N. Ghazzal, *Chem. Mater.* **2021**, *33*, 6925.
[58] K. E. Shopsowitz, H. Qi, W. Y. Hamad, M. J. MacLachlan, *Nature* **2010**, *468*, 422.
[59] M. Knezevic, T.-H. Hoang, C. Wang, M. Johar, A. G. Manjón, D. L. Rauret, C. Scheu, M. Erard, D. Berardan, J. Arbiol, *Adv. Mater. Interfaces* **2024**, *11*, 2300636.
[60] S. Zhou, Y. Liu, J. Li, Y. Wang, G. Jiang, Z. Zhao, D. Wang, A. Duan, J. Liu, Y. Wei, *Appl. Catal., B* **2014**, *20*, 158.
[61] J. Liu, T. Zhang, Z. Wang, G. Dawson, W. Chen, *J. Mater. Chem.* **2011**, *21*, 14398.
[62] C. Wang, X. Han, Q. Xu, Y.-N. Sun, J. Arbiol, M. N. Ghazzal, J. Li, *J. Mater. Chem. A* **2023**, *11*, 3380.
[63] C. Wang, J. Li, E. Paineau, H. Remita, M. N. Ghazzal, *Sol. RRL* **2023**, *7*, 2200929.

© 2024 The Authors. Advanced Materials Technologies published by Wiley-VCH GmbH

[64] M. Shi, D. Bao, B. Wulan, Y. Li, Y. Zhang, J. Yan, Q. Jiang, *Adv. Mater.* **2017**, *29*, 1606550.
[65] M. N. Ghazzal, N. Chaoui, M. Genet, E. M. Gaigneaux, D. Robert, *Thin Solid Films* **2011**, *520*, 1147.
[66] T. Aoki, *Opt. Prop. Mater.Appl.* **2019**, 157, https://doi.org/10.1002/9781119506003.ch6.
[67] Y. Ma, X. Wang, Y. Jia, X. Chen, H. Han, C. Li, *Chem. Rev.* **2014**, *114*, 9987.
[68] W. Zhang, M. Zhang, Z. Yin, Q. Chen, *Appl. Phys. B* **2000**, *70*, 261.
[69] H. Zhao, Z. Hu, J. Liu, Y. Li, M. Wu, G. Van Tendeloo, B.-L. Su, *Nano Energy* **2018**, *47*, 266.

© 2024 The Authors. Advanced Materials Technologies published by Wiley-VCH GmbH